Polarization-dependent spectra in the photoassociative ionization of cold atoms in a bright sodium beam

Jaime Ramirez-Serrano,* William DeGraffenreid,† and John Weiner‡
Laboratory of Atomic, Molecular, and Optical Science and Engineering, University of Maryland, College Park, Maryland 20742
(Received 29 October 2001; published 8 May 2002)

We report measurements of cold photoassociative ionization (PAI) spectra obtained from collisions within a slow, bright Na atomic beam. A high-brightness atom flux, obtained by optical cooling and focusing of the atom beam, permits a high degree of alignment and orientation of binary collisions with respect to the laboratory atom-beam axis. The results reveal features of PAI spectra not accessible in conventional magneto-optical trap studies. We take advantage of this high degree of alignment to selectively excite autoionizing doubly excited states of specific symmetry.

DOI: 10.1103/PhysRevA.65.052719 PACS number(s): 32.80.Fb, 33.80.Eh, 32.80.Pj, 33.80.Ps

I. INTRODUCTION

The study of cold collisions in samples of optically cooled and confined atoms has been an active area of research since Gould *et al.* [1] observed the first photoassociative ionization collisions in a dipole trap. Magneto-optical traps (MOTs) and far-off-resonance traps have provided ''reaction cells'' at temperatures well below 1 mK, and densities equal to or above 10^{10} cm^{-3}. Under these conditions of temperature and density only a few partial waves contribute to a binary collision event [2]. Trap experiments have been used to study in detail various collisional processes including photoassociation (PA) and the two-step photoassociative ionization (PAI) of cold atoms,

$$\mathrm{Na}(^2S_{1/2})+\mathrm{Na}(^2S_{1/2})+\hbar\omega_1\rightarrow \mathrm{Na}_2^*, \quad (1)$$

$$\mathrm{Na}_2^*+\hbar\omega_2\rightarrow[\mathrm{Na}_2^{**}]\rightarrow \mathrm{Na}_2^+ + e. \quad (2)$$

Atom trap measurements, however, spatially average over the molecular axis with respect to the laboratory reference frame and obscure effects due to the alignment or orientation of the colliding partners. In contrast, collisions within a dense well-collimated atomic beam can reveal these properties when the collision mechanism leads to a close alignment between the molecular and laboratory axes. Under these conditions the laboratory polarization axes of laser beams carrying $\hbar\omega_1$ and $\hbar\omega_2$ can be well-defined with respect to the molecular collision axis.

Up to now no PAI spectra exhibiting alignment and orientation information have been measured in atomic beams due to their low density and relatively high divergence. However, DeGraffenreid *et al.* [3,4] recently developed a dense, optically brightened beam specifically to meet the requirements of collision studies. In addition to low angular divergence (high brightness) combined with low velocity dispersion (high brilliance) the atom-beam density of $(1\pm0.5)\times10^{10}$ cm^{-3} is comparable to that obtained in conventional MOTs. This arrangement produces an intrabeam PAI collision rate sufficient for high-resolution photoassociation spectroscopy.

II. BEAM KINEMATICS

In general, even if an atomic beam is very bright and brilliant, collisions within it will be subject to spatial averaging if the final scattering state permits a wide acceptance angle of the incoming flux. However, as shown in the Newton diagram [10] of the top panel in Fig. 1, for the class of collisions involving long-range excitation, including the one-color ($\omega_1=\omega_2$) PAI process in sodium [2,5–8] considered here, the range of possible molecular collision axes is restricted to a narrow acceptance angle Θ determined by the two-step mechanism of PAI.

In the first step, optical excitation of the quasimolecule ($\hbar\omega_1$) takes place at large internuclear separation R_e, of the

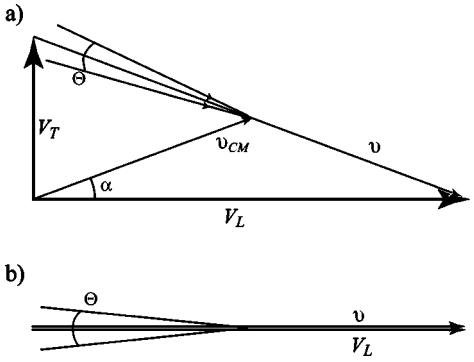

FIG. 1. Top panel: Newton diagram of a binary collision between two particles of equal mass. Note that the center-of-mass coordinate is located midway along the relative velocity vector. Laboratory longitudinal and transverse velocities are labeled V_L and V_T, respectively. The molecular acceptance scattering is labeled Θ. The center-of-mass velocity and angle are labeled $v_{\mathrm{c.m.}}$ and α, respectively. Bottom panel: Newton diagram showing how, as $V_T\rightarrow0$, the small Θ acceptance angle in the molecular frame aligns along the laboratory beam axis.

*Present address: Jet Propulsion Laboratory, Quantum Sciences Group, 4800 Oak Grove Drive, MS 298-100, Pasadena, CA 91104.
†Present address: Atomic Physics Division, National Institute of Standards and Technology, Gaithersburg, MD 20899-8421.
‡Present address: Université Paul Sabatier, IRSAMC-LCAR, 118 route de Narbonne, 31062 Toulouse, France.

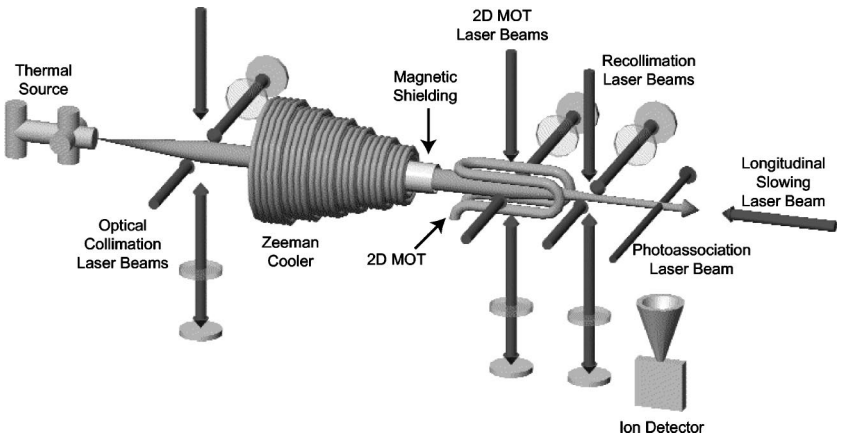

FIG. 2. Schematic of bright beam apparatus. See text for summary descriptions of major components.

order of several 100 Bohr radii (a_0). In the second step autoionization of the doubly excited molecular states occurs at a short distance R_c of the order of a few a_0. The angle Θ is defined by R_e/R_c, of the order of tens of milliradians. The Newton diagram in the bottom panel of Fig. 1 illustrates how a narrow range of Θ's can be exploited to advantage in collisions within an atomic beam. In the bright cold atomic beam reported here, laboratory transverse velocity components V_T, of the order of 1 m/s or less, are small compared to the longitudinal velocity V_L, of the order 350 m/s. The center-of-mass velocity $v_{\mathrm{c.m.}}$ for a pair of atoms diverges from the laboratory longitudinal beam axis by a small angle α, defined by $v_{\mathrm{c.m.}_T}/v_{\mathrm{c.m.}_L}$ and equal to V_T/V_L for particles of equal mass. The small angular divergence of both the relative velocity v in the molecular frame and the atom-beam velocity V in the laboratory frame ensure that their axes are superposed and aligned along the longitudinal axis of the atom beam to within a few tens of milliradians [9]. In fact it is easy to show that in the limit of $\alpha \ll \Theta$ and for binary association collisions with equal masses, the scattering angle in the laboratory frame becomes equal to Θ. Laser light intersecting the atom beam at right angles, with polarization aligned parallel or perpendicular to the atomic beam in the laboratory reference frame is, therefore, also closely aligned to the collision axis in the molecule reference frame.

III. EXPERIMENTAL APPARATUS

A. Summary description

The experiments are carried out using the atomic beam apparatus described in detail in Ref. [4] and shown in Fig. 2. Here we summarize the principal components: alkali vapor source, transverse optical molasses cooling, longitudinal Zeeman cooling, two-dimensional (2D) MOT ''extrusion,'' and PAI collision zone.

An externally heated oven assembled primarily from off-the-shelf UHV components generates the thermal beam. High-temperature custom fitted mantles heat sodium metal inside a reservoir made from a standard 4.5-in-diameter Conflat-style (CF) tee to about 400 °C. The reservoir is connected to a standard six-way CF cross. A skimmer-nozzle configuration, consisting of two thin stainless steel 1.25-mm apertures separated by 16 cm, mechanically restricts the atomic beam to a divergence angle of 8 mrad and limits the transverse velocity, at this oven temperature, to less than 10 m/s. A separate heating mantle, enveloping the cross, heats the nozzle and skimmer to 400 °C to prevent clogging. The beam source is connected to the main chamber by a flexible bellows that provides for beam pointing.

The transverse velocity components are further reduced by optical molasses cooling. A pair of counterpropagating laser beams, orthogonal to the atom beam and to each other, polarized in the ''lin $\perp$ lin'' configuration [11], i.e., with the two polariztion axes mutually or thougonal, enter the vacuum chamber through orthogonal windows on a six-way cross located 10 cm downstream from the skimmer. As described by DeGraffenreid *et al.* [4] we find that spatially offsetting the pair of molasses laser beams, creating *two* 1D molasses rather than *one* 2D molasses, prevents interferences and increases the average density by a factor of 2. Stray magnetic fields in the optical collimation region must be reduced to less than 1 G for efficient sub-Doppler cooling. Stray magnetic fields from the upstream end of the Zeeman slower are attenuated to $\simeq 0.1$ G by a combination of several sheets of high-permeability magnetic shielding material and a pair of Helmholtz coils.

The residual transverse velocity of the sodium beam after the optical collimation stage is estimated using a time-of-flight technique. We measure the atom-beam diameter with high-resolution charged-coupled device (CCD) images of resonance fluorescence at the point of optical collimation and at a point 2.0 m downstream. From the flight time (2.3 ms), determined from the average velocity of the thermal beam (850 m/s), and the measured beam divergence over the 2.0-m flight path, we estimate residual transverse velocity components of $\simeq 20$ cm/s, corresponding to a transverse atom-beam temperature of $\simeq 55$ μK.

The optically collimated sodium beam, with a thermal longitudinal and sub-Doppler transverse velocity distributions, enters the region where cooling along the atom-beam axis occurs. A laser beam with σ^+ polarization propagates coaxially and antiparallel to the atom beam. A conventional tapered solenoid, with the high-field end at the upstream end of the chamber, produces a longitudinal magnetic-field profile appropriate to maintain resonant absorption as the atoms decelerate and cool. Low laser intensity at the upstream end of the Zeeman slower inhibits efficient cooling of the fastest

atoms. To increase the intensity of the cooling laser at the upstream end, we focus the laser beam with a pair of lenses in a ''near telescope'' configuration, which overcomes the loss in cooling-laser photon flux by decreasing the laser beam cross section. The focus of the cooling laser is adjusted with the lenses to get the highest flux of cooled atoms at the exit of the solenoid.

Cold collision studies require low *relative* velocities (<5 m/s) between pairs of atoms. To produce an ensemble of coaxially moving atoms with small relative speed, the laboratory distribution of velocities must be narrow. Slowing the atoms to near zero velocity in the laboratory frame actually increases the distribution because the magnetic field at the end of the tapered solenoid does not exactly match the field shape needed for cooling. Rapid removal from the cooling cycle at a well-defined velocity upstream from the end of the solenoid produces an atom beam with a narrow longitudinal velocity spread. Atoms will exit the cooling cycle [12] if the field gradient exceeds

$$\left|\frac{dB}{dz}\right|_{crit} = \frac{1}{v_{0\|}} \frac{\hbar|\vec{k}|^2}{2\tau\mu_B m} \frac{S}{S+1}, \tag{3}$$

where $v_{0\|}$ is the longitudinal atom velocity at the decoupling point, τ is the excited-state lifetime, μ_B is the Zeeman constant, m is the sodium atomic mass, and S is the saturation parameter ($=I/I_0$) with I_0 the resonance transition saturation power density. We shape the field cutoff with an assembly of magnetic shielding. Multiple layers of a high-permeability nickel alloy foil, wrapped into a cylindrical tube 10 cm in length form the assembly. The structure, mounted coaxially with the atom beam and within the downstream end of the solenoid, abruptly shields the atoms from the Zeeman cooling field. The terminal longitudinal velocity is determined by the resonant condition at the site of decoupling. For the experimental conditions described here, the gradient increases to a maximum value of 140 G/cm at the edge of the shielding, well above the critical value of 30 G/cm given by Eq. (3), and atoms decouple from the cooling cycle with a velocity $v_{\|}$ of 350 m/s. We measure [4] the laboratory-frame longitudinal velocity dispersion $\Delta v_{\|}$ to be 5 m/s.

To further increase the brightness of the atom beam, the flux must be compressed into a smaller volume, without increasing the divergence of the beam at the same time. A two-step process, utilizing atom-beam focusing followed by optical collimation, reduces the beam diameter from 2 mm to 0.6 mm without loss of collimation. The focusing stage of this ''atom-beam extruder'' is a 2D MOT. A hairpin assembly generates the extruder magnetic field. Four sections of wires, with alternating directions of current, produce the quadrupole field. The straight sections of wire are 5 cm long and 1 cm offset from nearest neighbors. Similar to the upstream end of the Zeeman cooler, a pair of coaxial Helmholtz coils cancels the fringing fields from the Zeeman slower solenoid. The 2D MOT focuses the atom beam to a point downstream from the extruder assembly. The exact focal point depends on the field gradient and on the longitudinal velocity of the beam. The narrow velocity distribution produced by the rapid cutoff of the longitudinal Zeeman magnetic field results in a small chromatic aberration of the focal length (~ 1 mm). For a beam with $v_{\|}=350$ m/s and a hairpin current of 45 A, the focal point is about 6 cm downstream from the 2D-MOT laser beams. To prevent atom-beam divergence beyond the focal point, an optical recollimation stage introduced at the focus damps out the transverse velocity acquired from focusing. The lin$\perp$lin optical molasses stage, using light produced by the same laser as the primary optical collimation and the 2D MOT, is 2 cm in length and positioned at the focus of the atom beam. The same Helmholtz coils used to cancel the fringe fields in the focusing stage also cancel the magnetic field at the collimation stage to $|B|<1$ G, allowing sub-Doppler cooling mechanisms in the molasses to reduce the transverse temperature to $T_{\perp} \sim 55$ μK, below the Doppler limit ($T_D=240$ μK). The extruder acts essentially as an atom-beam telescope, reducing the beam radius Δr from 1 mm, at the end of the Zeeman cooler, to 0.3 mm at the extruder exit, based on measurements of the beam fluorescence collected with a CCD camera. The beam current J (atoms s^{-1}) entering the extruder equals the exiting current, indicating that essentially all atoms are forced into the narrowed beam.

TABLE I. Summary of beam characteristics.

n	Density (atoms/cm^3)	$(1\pm0.5)\times10^{10}$
$v_{\|}$	Longitudinal velocity (m/s)	350 ± 5
$\Delta v_{\|}$	Longitudinal velocity spread (m/s)	5 ± 1
$\Delta v_{\perp}$	Transverse velocity spread (m/s)	0.25 ± 0.1
Ω	Solid angle (sr)	$(2\pm1)\times10^{-6}$
Δr	Beam radius (cm)	0.03 ± 0.01

B. Performance

We determine the properties of the beam 2.2 m downstream from the skimmer, at the point where our cold collision experiments are performed. Adding just the first optical collimation stage to the longitudinally cooled beam increases the density from 2×10^7 cm^{-3} to 7×10^8 cm^{-3}. The extruder further increases the density to 1×10^{10} cm^{-3}, a combined 500-fold density gain. The beam-divergence solid angle $\Omega=\pi(\Delta v_{\perp}/v_{\|})^2$ decreases from 1×10^{-4} sr to 2×10^{-6} sr as the thermal beam is collimated, cooled, and extruded. Table I summarizes the beam parameters within which the intrabeam cold collisions take place.

C. Collision temperature

We define a collision ''temperature'' by determining the *relative* velocity distribution and average collision velocity within the atom beam. To measure the longitudinal velocity distribution of the atom beam, a weak probe beam ($I<I_{sat}$), introduced at an angle ϕ with respect to the atom beam, scans near the rest-frame atomic resonance. The Doppler-shifted, angle-tuned resonant absorption condition is given by

$$\Delta\omega = \omega_0 - \frac{2\pi v_{\|}}{\lambda}\cos\phi, \tag{4}$$

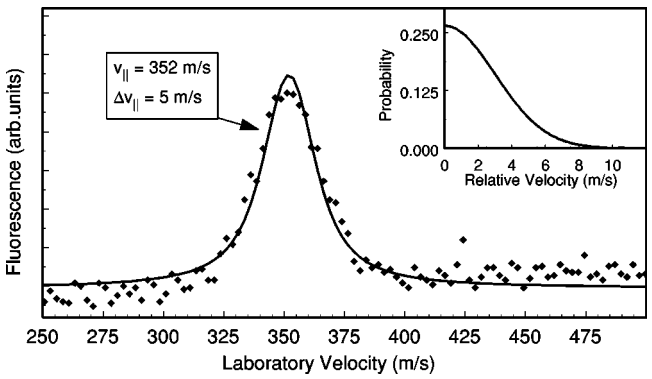

FIG. 3. Voigt fit to fluorescence line shape from which laboratory velocity distribution is numerically determined. The atom laboratory velocity distribution in turn is used in Eq. (7) to calculate the relative collision velocity distribution in the atom beam.

where $\Delta\omega$ is the detuning from resonance at which atoms with velocity $v_{\|}$ absorb. A photomultiplier tube registers fluorescence from atoms Doppler-shifted into resonance with the detuned light. We extract the velocity distribution $f(v')$ from the line width $g(v)$, by fitting a Voigt profile

$$I(v)=I_o\int f(v')g(v-v')dv' \tag{5}$$

to the spectra. We assume a 1D Gaussian distribution of velocities for $f(v')$. The probe laser intensity and the center velocity of the fluorescence are known, leaving the longitudinal velocity spread $\Delta v_{\|}$ and a normalization constant as the only remaining parameters to fit. A typical fit, with a laboratory velocity width $\Delta v_{\|}$ equal to 5 m/s, is shown in Fig. 3.

The collision temperature T_{coll} for a pair of atoms depends on the relative velocity v_r between them:

$$kT_{coll}=\frac{1}{2}\mu\langle v_r\rangle^2. \tag{6}$$

An autocorrelation of the laboratory distributions, $f(v_1)$ and $f(v_2)$, for two atoms

$$P_r(v_r)=\int_0^\infty\int_0^\infty f(v_1)f(v_2)\delta(v_r-|v_1-v_2|)dv_1v_2 \tag{7}$$

determines the relative velocity distribution $P_r(v_r)$ of a colliding pair in the beam. The inset of Fig. 3 shows $P(v_r)$ for two atoms in the atom beam. We calculate the average relative velocity from the relative velocity distribution

$$\langle v_r\rangle=\int_0^\infty P_r(v_r)v_rdv_r. \tag{8}$$

For the typical data shown in Fig. 3, the mean relative velocity $\langle v_r\rangle$ is 2.4 m/s and the collision temperature T_{coll} is 4 mK.

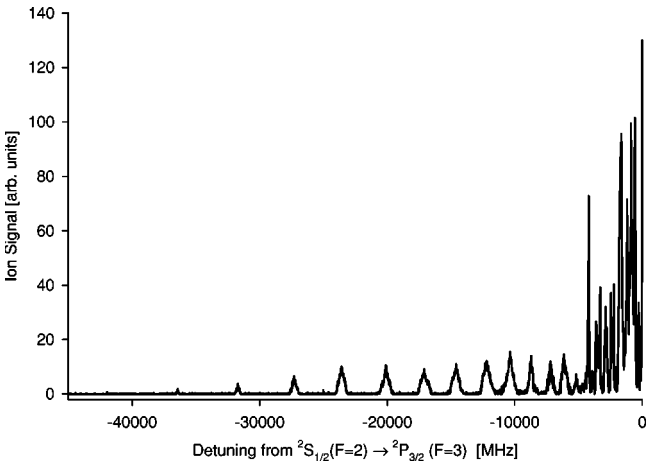

FIG. 4. Photoassociative ionization spectra for parallel polarization over the range of measurements (0–45)-GHz detuning to the red region of resonance.

IV. PHOTOASSOCIATIVE IONIZATION SPECTRA

The PA laser intersects the atom beam at right angles in the interaction zone a few centimeters downstream from the extruder. To obtain the PAI spectrum as a function of laser detuning, the PA laser frequency is scanned in 10-MHz steps to the red region of the $3\,^2S_{1/2}(F=2)\rightarrow 3\,^2P_{3/2}(F=3)$ atomic line over a range of 45 GHz. The $Na_2{}^+$ ions produced are counted during a 10-s interval, and the procedure is repeated at every detuning step for each of the three polarization cases: linear polarization parallel and perpendicular to the atom beam as well as circular polarization. In all cases the light propagation direction is orthogonal to the atom beam. The PA laser is first calibrated to a known frequency by using the absorption signal from an iodine cell, together with a feature from the saturation absorption spectrum of sodium.

Ion spectra covering the entire range from 0 to -45 GHz are shown in Fig. 4. As has been described in earlier MOT experiments [5–8], the spectra show a congested region from 0 to 5 GHz followed by a regularly spaced progression with slowly varying amplitude. The spectra in Figs. 5 and 6 show in more detail these two regions. Figure 6 also compares the beam results from the ''first 5 GHz'' to a similar one-color spectrum obtained from a conventional MOT [7,8]. The peak heights of the beam spectra have been normalized to those of the MOT spectra at the peak near -4.2 GHz.

The beam measurements exhibit characteristics similar to the MOT results with three significant differences: the spectra show a marked polarization dependence on the peak amplitudes, a slightly improved spectral resolution over the MOT results, and new peaks within a detuning range from 0 to 750 MHz where the PA laser beam destabilizes a MOT.

A. Polarization analysis in the first 5 GHz

In the first 5 GHz detuning, the two-step PAI process consists of an initial excitation to a ''pure long-range'' state [13] of 0_g^- symmetry, followed by a second step that trans-

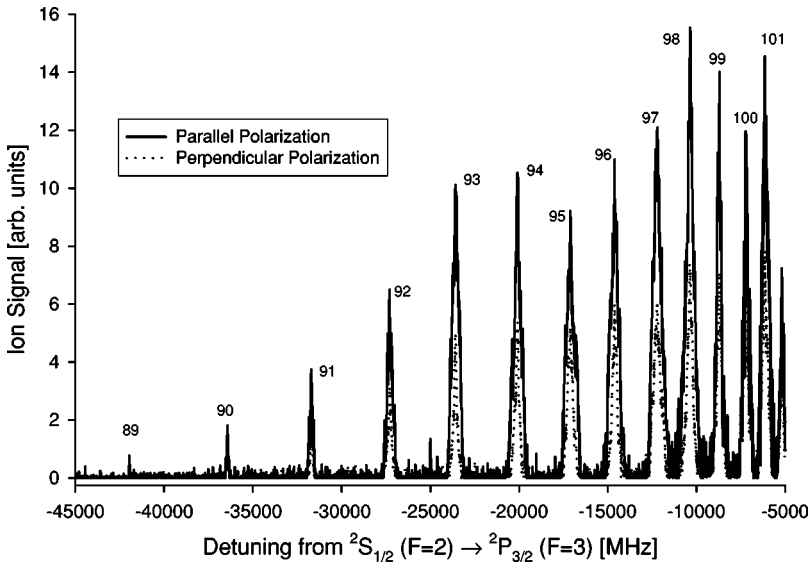

FIG. 5. Bright beam PAI spectra in the region from 5 to 45 GHz to the red region of the $3S_{1/2}(F=2) \rightarrow 3P_{3/2}(F=3)$ resonance. Solid trace, parallel polarization; dotted trace, perpendicular polarization. Numbered peaks label vibrational levels of the 1_g intermediate state.

fers population to the doubly excited state of either 1_u or 0_u^- symmetry [8]. The doubly excited state subsequently autoionizes at short range. Since the first excitation step must pass through a 0_g^- state, dipole selection rules dictate that the starting ground molecular state must be of 1_u or 0_u^- symmetry, corresponding to components of the familiar $Na_2\ ^3\Sigma_u$ lowest triplet (''ground'') state in Hund's case (b) notation.

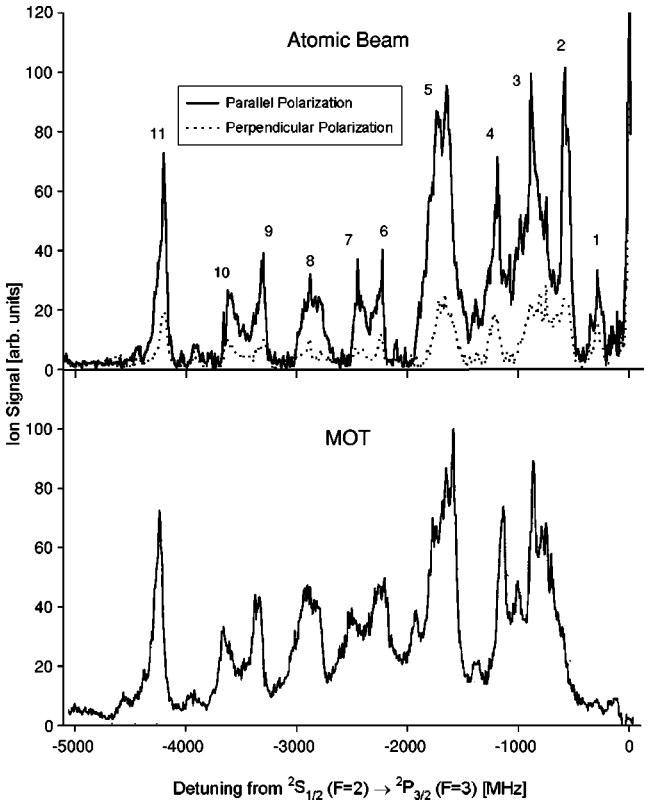

FIG. 6. Top panel: Bright beam PAI spectra within the first 5 GHz detuning to the red region of resonance. Solid trace is parallel polarization. Dotted trace is perpendicular polarization. Peak numbered labels are for reference only. Bottom panel: PAI spectra obtained from a conventional MOT, [7,8].

Electric dipole transitions in which the quantum number for the total electronic angular-momentum projection along the quantization axis is unchanged or differs by one unit, $\Delta\Omega = 0(\pm 1)$, are called parallel (perpendicular) transitions because the molecular states are coupled by the dipole transition moment parallel (perpendicular) to the quantization axis. Hence, PA light with parallel (perpendicular) polarization only couples the 0_u^- (1_u) ground states to the intermediate 0_g^- state. Starting from the common 0_g^- intermediate state, parallel (perpendicular) polarized light populates the doubly excited state 0_u^- (1_u) symmetry. Thus, as summarized in Fig. 7, light polarized parallel or perpendicular to the atom-beam axis populates selectively the doubly excited state of either symmetry from the ground state.

However, in the specific laboratory setup reported here, where the probe beam propagates orthogonal to the atom beam, and the polarization axis is aligned either parallel or perpendicular to the atom beam, the excitation *rate* for these two types of transitions is not identical. It is easy to see why by considering the three Cartesian components of the transition moment $\boldsymbol{\mu}$ with the μ_z aligned along the molecular internuclear axis and with μ_x, μ_y perpendicular. With **E** the electric field of the polarized PA probe light, the excitation rate from the ground molecular state $|g\rangle$ to the 0_g^- interme-

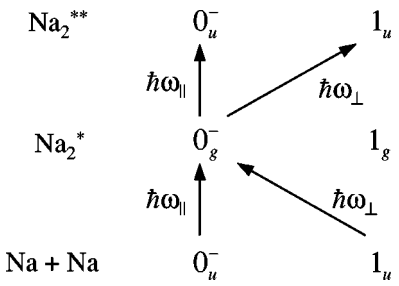

FIG. 7. Schematic diagram showing how two successive parallel or perpendicular transitions, passing through the 0_g^- intermediate state, selectively populate the 0_u^- or 1_u doubly excited states in the region of (0–5)-GHz detuning.

diate excited state $|e\rangle$ is proportional to the dipole coupling matrix element, expressed as

$$\langle g|\mathbf{E}\cdot\boldsymbol{\mu}|e\rangle=\langle g|E_x\mu_x|e\rangle+\langle g|E_y\mu_y|e\rangle+\langle g|E_z\mu_z|e\rangle. \tag{9}$$

The PA light propagates at right angles to the atom beam and is linearly polarized along z (parallel polarization) or along x (perpendicular polarization). For parallel transitions

$$E_\parallel\mu_\parallel=E_z\mu_z \tag{10}$$

and, in general, for perpendicular transitions

$$E_\perp\mu_\perp=E_x\mu_x+E_y\mu_y. \tag{11}$$

For an atom in isotropic space it is clear that

$$\mu_x=\mu_y \quad \text{and} \quad \mu_\perp=\mu_\parallel \tag{12}$$

and, therefore,

$$\langle g|E_x\mu_x|e\rangle=\langle g|E_y\mu_y|e\rangle=\frac{1}{2}\langle g|E_z\mu_z|e\rangle. \tag{13}$$

Since in the experimental arrangement the perpendicularly polarized PA light beam excites only the μ_x component, the coupling rate for perpendicular transitions from the ground to the intermediate states, $k_{1_\perp}$, is half of that of parallel transitions, $k_{1_\parallel}$.

A similar result holds for the rate of the second excitation step, $k_{2_\parallel}$ ($k_{2_\perp}$), transferring population from the 0_g^- excited state $|e\rangle$ to the 0_u^- (1_u) doubly excited states $|ee\rangle$. The overall population rate for each of the two doubly excited states is a product of the rates of the two successive steps. Therefore, assuming that the state symmetry labels for the two doubly excited states are correct, the overall population rate of the doubly excited 0_u^- state, proceeding through two parallel transitions, $(k_1k_2)_\parallel$, should be four times faster than the rate $(k_1k_2)_\perp$ populating the doubly excited 1_u state.

The rate equation describing the net time rate of population change in the doubly excited states is given by

$$\frac{dN^{**}_{0_u^-}}{dt}=(k_1k_2)_\parallel N_g-k_{0_u^-}N^{**}_{0_u^-} \tag{14}$$

and

$$\frac{dN^{**}_{1_u}}{dt}=(k_1k_2)_\perp N_g-k_{1_u}N^{**}_{1_u}, \tag{15}$$

where $k_{0_u^-}$ and k_{1_u} are the rate constants for loss from the doubly excited states and $N^{**}_{1_u}$, $N^{**}_{0_u^-}$, N_g are the populations of the doubly excited and ground states. This loss is the sum of associative ionization and radiative decay. The time of flight from the Condon point for the second-step excitation to the inner zone, where associative ionization takes place (~ 0.5 ns) is sufficiently rapid, so that losses from spontaneous emission can be neglected. At steady state we then have

$$(k_1k_2)_\parallel N_g=k^{ai}_{0_u^-}N^{**}_{0_u^-} \quad \text{and} \quad (k_1k_2)_\perp N_g=k^{ai}_{1_u}N^{**}_{1_u} \tag{16}$$

and, therefore,

$$\frac{(k_1k_2)_\parallel}{(k_1k_2)_\perp}=\frac{k^{ai}_{0_u^-}N^{**}_{0_u^-}}{k^{ai}_{1_u}N^{**}_{1_u}}=\frac{I_\parallel}{I_\perp}=4. \tag{17}$$

However, the right-hand side of Eq. (17) represents the relative associative ionization rate from the two doubly excited states, if we only take into account rate differences due to the orientation of the transition moment. In fact the excitation routes in Fig. 7 show that the second step should populate *either* the 0_u^- state (parallel polarization) *or* the 1_u state perpendicular polarization. Therefore, we would expect those peaks in Fig. 6 associated with $0_g^-\rightarrow 0_u^-$ to appear only with parallel polarization, and the remaining peaks associated with $0_g^-\rightarrow 1_u$ to appear only with perpendicular polarization. In fact very nearly the same set of peaks appears with excitation by both polarizations, but with quite different intensities. Table II lists the measured intensity ratios for the 11 peaks numbered in Fig. 6 together with doubly excited state symmetry labels assigned from the the spectroscopic analysis of Amelink *et al.* [7,8]. Thus we would expect peaks 3,5,9,10,11 to appear only with parallel polarization and peaks 1,2,6,7,8 to appear only with perpendicular polarization. Nevertheless, it is clear that all peaks appear with both polarization and that parallel transitions are always more intense than perpendicular transitions.

These results lead to the conclusion that the actual autoionizing molecular states may not be well characterized by the symmetry labels 0_u^- and 1_u, but may be some linear combination of the two. If we postulate a mixed state

TABLE II. Relative ion yields for the 11 prominent peaks with (0–5)-GHz detuning. The relative yields are listed as $I\parallel/I\perp$. The state symmetry assignments are inferred from the spectroscopic analysis of Amelink *et al.* [7,8].

Peak number	Detuning (GHz)	$\frac{I\parallel}{I\perp}$	State label
1	0.290	2.00	1_u
2	0.580	2.78	1_u
3	0.890	3.30	0_u^-
4	1.190	3.93	?
5	1.700	4.47	0_u^-
6	2.230	3.27	1_u
7	2.450	3.70	1_u
8	2.880	3.41	1_u
9	3.310	3.03	0_u^-
10	3.600	2.66	0_u^-
11	4.150	3.24	0_u^-

TABLE III. Numbered peaks, (0–5)-GHz detuning and mixing coefficients C_1/C_2.

Peak number	$\frac{I_\parallel}{I_\perp}$	C_1/C_2
1	2.00	0.71
2	2.78	0.83
3	3.30	0.91
4	3.93	0.99
5	4.47	1.06
6	3.27	0.90
7	3.70	0.96
8	3.41	0.92
9	3.03	0.87
10	2.66	0.82
11	3.24	0.90

$$\psi = C_1|0_u^-\rangle + C_2|1_u\rangle \tag{18}$$

with mixing coefficients C_1, C_2, the population probabilities (and hence the PAI rates) are given by

$$\frac{I_\parallel}{I_\perp} = 4\frac{|C_1|^2}{|C_2|^2}, \tag{19}$$

where the factor of 4 comes from Eq. (17). If the two states were equally mixed, we would expect an intensity ratio of 4. In fact Eq. (19) can be used to determine the relative mixing coefficients. Table III lists the numbered peaks, the relative PAI intensity, and the ratio of the mixing coefficients. It appears that the two states are strongly mixed and that most of the polarization effect is due to the Clebsch-Gordan factors expressed by Eq. (17).

Amelink *et al.* [7] analyzed linewidths of two-color PAI spectra. These authors, comparing the highest vibrational levels for each doubly excited state and measuring peak widths, found relative autoionization rates $1_u/0_u^- \simeq 1.4$–1.6 with a trend toward more rapid autoionization as vibrational energy decreases. Table III of Ref. [7] indicates that autoionization rates increase somewhat faster for the 1_u state compared to the 0_g^- state as a function of decreasing vibrational energy. The one-color results reported here, however, cannot be compared directly to the two-color measurements of Ref. [7], since, for any given one-color detuning, different vibrational levels of the two doubly excited states will be populated.

B. Analysis of results in the region beyond the first 5 GHz

Previous work in MOTs [5,6,8] have assigned the regular peak progression in the PAI spectrum beyond the first 5 GHz to a singly excited state of 1_g symmetry. In this region (Fig. 5) PAI does not proceed through the 0_g^- pure-long-range intermediate state but through a chemically bound 1_g state with inner turning point $\sim 25a_0$. As the probe laser is tuned to the red region from 5 GHz to 45 GHz, the atoms colliding on the 1_u or 0_u^- ground states undergo transitions around the

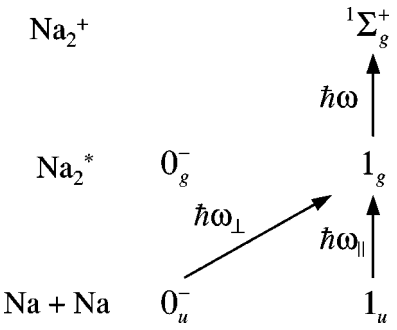

FIG. 8. Schematic diagram showing how parallel or perpendicular transitions, passing through the 1_g intermediate state, directly photoionize to the Na_2^+ ground state in the PAI detuning region to the red region of 5 GHz.

Condon points corresponding to the outer turning points of the vibrational states associated with this 1_g electronic state. At the inner turning point, a second transition photoionizes the Na_2^* 1_g population to Na_2^+. According to this conventional interpretation we expect the polarization-dependent ion yield for parallel polarized probe light to be twice that for perpendicular polarization. Figure 8 illustrates the two pathways. Table IV lists the measured relative intensities for 11 peaks in the detuning range 6 to 32 GHz. The ion yield ratio, averaged over the 11 peaks, is 1.95 ± 0.06, in good agreement with the expected result.

V. SUMMARY AND CONCLUSIONS

We have reported the PAI spectra resulting from photoassociation collisions in a cold, bright atom beam. The analysis of the polarization dependence in the detuning range from 5–45 GHz to the red region of the dissociation limit is consistent with the steps depicted in Fig. 8, one-step photoassociation to the 1_g intermediate state followed by direct photoionization to the molecular ion. In contrast, the polarization-dependent spectra within the first 5 GHz of red region detuning indicates that the 1_u and 0_u^- doubly excited states

TABLE IV. Numbered peaks in the (5–45)-GHz detuning range and relative ion yield ($I_\parallel/I_\perp$) for PAI spectrum.

Peak number	Detuning (GHz)	$\frac{I_\parallel}{I_\perp}$
101	6.10	1.88
100	7.20	1.71
99	8.70	2.00
98	10.35	2.07
97	12.20	2.00
96	14.60	1.83
95	17.10	1.77
94	20.10	2.02
93	23.58	2.02
92	27.3	2.10
91	31.70	2.06

may be strongly mixed by hyperfine and rotational coupling [14].

This study of PAI within a cold bright beam illustrates how the rate of photoassociation in an aligned atomic collision can be made sensitive to the linear polarization of the photoassociating field. Spin orientation of the colliding partners in these essentially one-dimensional collisions can also be used to modify dramatically the rate of molecule formation.

ACKNOWLEDGMENTS

Financial support from the National Science Foundation, the Army Research Office, and the National Institute of Science and Technology is gratefully acknowledged.

[1] P.L. Gould, P.D. Lett, P.S. Julienne, W.D. Phillips, H.R. Thorsheim, and J. Weiner, Phys. Rev. Lett. **60**, 788 (1988).

[2] For a review of cold and ultracold collisions see, J. Weiner, V.S. Bagnato, S. Zilio, and P.S. Julienne, Rev. Mod. Phys. **71**, 1 (1999).

[3] W. DeGraffenreid, J. Ramirez-Seranno, Y.-M. Liu, A. Rosenbaum, and J. Weiner, J. Appl. Phys. **B71**, 881 (2000).

[4] W. DeGraffenreid, Y.-M. Liu, J. Ramirez-Serrano, and J. Weiner, Rev. Sci. Instrum. **71**, 3668 (2000).

[5] P.D. Lett, K. Helmerson, W.D. Phillips, L.P. Ratliff, S.L. Rolston, and M.E. Wagshul, Phys. Rev. Lett. **71**, 2200 (1993).

[6] L.P. Ratliff, M.E. Wagshul, P.D. Lett, S.L. Rolston, and W.D. Phillips, J. Chem. Phys. **101**, 2683 (1994).

[7] A. Amelink, K.M. Jones, P.D. Lett, P. van der Straten, and H.G.H. Heideman, Phys. Rev. A **61**, 042707 (2000).

[8] A. Amelink, K.M. Jones, P.D. Lett, P. van der Straten, and H.G.H. Heideman, Phys. Rev. A **62**, 013408 (2000).

[9] A. Amelink, Ph.D. thesis, Utrecht University, The Netherlands, 2000.

[10] U. Buck, in *Atomic and Molecular Beam Methods*, edited by G. Scoles (Oxford Press, New York, 1988), Vol. 1, pp. 449–456.

[11] J. Dalibard and C. Cohen-Tannoudji, J. Opt. Soc. Am. B **6**, 2023 (1989).

[12] R.J. Napolitano, S.C. Zilio, and V.S. Bagnato, Opt. Commun. **80**, 110 (1990).

[13] W.C. Stwalley, Y.-H. Uang, and G. Pichler, Phys. Rev. Lett. **41**, 1164 (1978).

[14] M. Elbs, O. Keck, H. Knöckel, and E. Tiemann, Z. Phys. D: At., Mol. Clusters **42**, 49 (1997).